Enhancing Atmospheric Water Harvesting of MIL-101 (Cr) MOF Sorbent with Rapid Desorption Enabled by Ni–Ni_3S_2 Photothermal Bridge

Chen, Weicheng; Liu, Yangxi; Xu, Bolin; Cheng, Bin; Ganesan, Muthusankar; Tan, Yuxuan; Luo, Mingyun; Chen, Bingzhi; Zhao, Xiaolong; Lin, Ci; Qin, Tingting; Luo, Fan; Fang, Yutang; Wang, Shuangfeng; Liang, Xianghui; Fu, Wanwan; Tan, Bingqiong; Ye, Ruquan; Leung, Dennis Y.C.; Ravi, Sai Kishore

Published in:
Advanced Functional Materials

Published: 23/12/2024

Document Version:
Final Published version, also known as Publisher's PDF, Publisher's Final version or Version of Record

Published version (DOI):
10.1002/adfm.202410999

Publication details:
Chen, W., Liu, Y., Xu, B., Cheng, B., Ganesan, M., Tan, Y., Luo, M., Chen, B., Zhao, X., Lin, C., Qin, T., Luo, F., Fang, Y., Wang, S., Liang, X., Fu, W., Tan, B., Ye, R., Leung, D. Y. C., & Ravi, S. K. (2024). Enhancing Atmospheric Water Harvesting of MIL-101 (Cr) MOF Sorbent with Rapid Desorption Enabled by Ni–Ni_3S_2 Photothermal Bridge. *Advanced Functional Materials*, *34*(52), Article 2410999. https://doi.org/10.1002/adfm.202410999

ADVANCED FUNCTIONAL MATERIALS
www.afm-journal.de

Enhancing Atmospheric Water Harvesting of MIL-101 (Cr) MOF Sorbent with Rapid Desorption Enabled by Ni—Ni_3S_2 Photothermal Bridge

Weicheng Chen, Yangxi Liu, Bolin Xu, Bin Cheng, Muthusankar Ganesan, Yuxuan Tan, Mingyun Luo, Bingzhi Chen, Xiaolong Zhao, Ci Lin, Tingting Qin, Fan Luo, Yutang Fang, Shuangfeng Wang, Xianghui Liang, Wanwan Fu, Bingqiong Tan, Ruquan Ye, Dennis Y.C. Leung,* and Sai Kishore Ravi**

Metal–organic frameworks (MOFs) have emerged as leading candidates for atmospheric water harvesting (AWH). Despite their high water uptake capacity, challenges persist in effective solar-driven desorption for water collection. Addressing this, a photothermal bridge is introduced by in situ growth of Ni_3S_2 coating on a thermally conductive nickel mesh, enhancing heat transfer to the MOF and accelerating desorption kinetics. MIL-101 (Cr) MOF in bulk form (BMOF) is bonded to the lightweight Ni—Ni_3S_2 mesh using adhesive, forming a dual-layer Ni—Ni_3S_2 mesh/BMOF assembly. This hybrid retains a high water uptake of ≈0.63 g g^{-1} at 60% relative humidity (RH) with superior sorption kinetics. Photothermally driven heat transfer from Ni—Ni_3S_2 to BMOF achieves complete water desorption within 40 min under 1 kW m^{-2}. Compared to other configurations like foil, granules, and foam, the mesh-based hybrid has the highest single-cycle adsorption–desorption kinetic of 3.18×10^{-3} g g^{-1} min^{-1}. Additionally, the hybrid demonstrates exceptional hydrothermal stability over 50 cycles and maintains morphological stability with airflow, ensuring consistent performance. Heat transfer simulations confirm the thermal distribution across the Ni—Ni_3S_2 mesh/BMOF, corroborating the rapid and uniform desorption. This approach paves the way for efficient AWH in high-RH, water-scarce regions by enhancing desorption kinetics through solar energy.

1. Introduction

The industrialization surge and burgeoning population have significantly ramped up the demand for freshwater, a situation exacerbated to the point that over 50% of the global population is projected to face water shortages by 2050.[1,2] The cause of water shortages varies in regions with different relative humidities (RHs). Many parts of the Middle East and Northern Africa endure desert climates characterized by low RH levels (below 30%) and high temperatures. Conversely, regions like Papua New Guinea, Mongolia, Laos, Pakistan, and Cambodia have high RH levels of ≈70% but grapple with over-industrialized surface waters that fall perilously below drinkable standards due to pollution.[3] To alleviate water shortages, techniques focusing on the desalination of seawater or polluted water have been proposed and are getting technologically mature, mainly using membrane-based or thermal processes to recycle water.[4,5]

W. Chen, B. Xu, B. Cheng, M. Ganesan, R. Ye, S. K. Ravi
School of Energy and Environment
City University of Hong Kong
Hong Kong, China
E-mail: skravi@cityu.edu.hk

The ORCID identification number(s) for the author(s) of this article can be found under https://doi.org/10.1002/adfm.202410999

DOI: 10.1002/adfm.202410999

W. Chen, Y. Liu, Y. Tan, M. Luo, B. Chen, F. Luo, Y. Fang, S. Wang, X. Liang, B. Tan
Key Laboratory of Enhanced Heat Transfer and Energy Conservation of the Ministry of Education
South China University of Technology
Guangzhou, China
E-mail: ceyxliu@mail.scut.edu.cn

W. Chen, X. Zhao, C. Lin, T. Qin, D. Y. Leung
Department of Mechanical Engineering
The University of Hong Kong
Hong Kong, China
E-mail: ycleung@hku.hk

W. Fu
School of Civil Engineering and Architecture
Wuhan Polytechnic University
Wuhan, China

While these desalination techniques have shown promise by providing high daily water yields, they come with significant downsides: they are energy-intensive, incur substantial costs, and their deployment is geographically constrained. These drawbacks make widespread adoption challenging, particularly in the least developed countries. These regions, hardest hit by water scarcity, often cannot afford such solutions due to economic limitations, thus exacerbating the dilemma of addressing global water shortages with current technologies.[6,7]

Fortunately, the emerging technology of sorption-based humidity harvesting presents a beacon of hope, offering a solution that is both low-cost and adaptable for small-scale, decentralized water generation. Leveraging the abundant and universally available atmospheric water, this technology breaks free from geographic limitations, fostering "water independence" at the household level.[8,9] Central to humidity harvesting are the sorbents, which play a pivotal role in water yield. These include zeolites, silicones, polymeric gels, hygroscopic metal–organic frameworks (MOFs), and salts.[10–12] Of these adsorbents, MOFs stand out for their low desorption temperatures, which allow for preliminary desorption through sunlight exposure. They also boast advantages such as hydrothermal stability and adjustable porosity.[13,14]

For tangible benefits in combating water scarcity, the sorption characteristics of MOFs must be tailored to address the diverse challenges posed by different regions. In arid locales with low RH, Yaghi et al. have demonstrated the potential of specific MOFs (MOF-303[15–17] and MOF-801[18,19]) in designing atmospheric water generators, showcasing promising commercial prospects at both material and device levels.[20] Despite their impressive sorption kinetics under sub-30% RH conditions, attributed to strong hydrophilicity, these MOFs exhibit relatively low saturated adsorption capacities. While in high RH regions, MOFs with higher adsorption capacity are preferred options, such as MIL-101 (Cr) and MIL-100 (Fe) with high specific surface areas of above 2000 $m^2\ g^{-1}$.[21,22] Particularly, MIL-101 (Cr) has been reported as one promising candidate for humidity harvesting in high RH regions, not only because of its high water uptake over 0.9 g g^{-1} (at 60% RH and 25 °C), but also because of its S-type water isotherm that allows for a steep increase in water uptake over 40% RH.[23] Nonetheless, commercially leveraging MOFs in humidity harvesting has challenges; the current desorption processes are hindered by slow and inadequate performances that curtail the daily water yield. This bottleneck, rooted either in inherent desorption attributes or limited sunlight availability, sees a rapid decline in desorption rates as the sorbent's water content reduces.[24] A further complexity arises from the uneven temperature distribution within the sorbents when exposed to sunlight, causing non-uniform desorption and extended desorption times.

To address this, several attempts have been made to integrate photothermal materials with sorbents, including photothermal semiconductors, plasmonic metals, and carbons. Semiconductors, in particular, are low-cost, exhibit excellent photothermal behavior, and offer environmental protection.[25] Based on this, various photothermal sorbents with different architectures have been synthesized, such as foil, foam, and granule structures. For instance, Tao et. al.[26] assembled a foam-structured photothermal sorbent by embedding metal foam (MF) into MOF monoliths (MF@MOFs) to enhance desorption. However, the water uptake of MF@MOFs decreased by more than 40% compared to pristine MOFs. Tan et al.[27] developed a foil-structured photothermal sorbent by growing Al-Fum MOF on a chitosan-embellished CuxS foil. Similarly, the water uptake of the assembled MOF (0.223 g g^{-1}) was reduced by 58.1% compared to the pristine MOF (0.532 g g^{-1}) at 25 °C and 90% RH. Moreover, the preparation process was complex. Direct contact of granule-MOF structures may cause issues such as low stability, insufficient light exposure (the bottom photothermal granules will be shaded), and blocked pores (the MOF pores may be blocked by photothermal granules).[28,29] Considering these limitations, developing a reasonable architecture for photothermal sorbents with high water uptake retention, high stability, and effective illuminated area is of significant importance.

Herein, we propose a strategy that entails the development of a "photothermal bridge" to facilitate effective and uniform desorption by capturing sunlight and transferring the photogenerated heat to the MOF sorbent. This is realized through the in situ growth of Ni_3S_2 photothermal particles on a thermally conductive Ni mesh. Compared with other reported semiconductors, such as Cu_xS,[28] Ag_2Se,[30] Ag_2S,[31] and NiO_x,[32,33] Ni_3S_2 simultaneously offers high performance, stability, and cost-effectiveness. Additionally, it can be easily grown in situ on Ni substrates. To evaluate the effects of this photothermal bridge, we chose MIL-101 (Cr), a material known for its desorption inefficiency, which manifests as incomplete desorption — it releases less than half of the trapped water in non-summer seasons[34] — and significantly prolonged desorption periods, extending to several hours under 1 kW m^{-2} illumination.[29] This MOF was preliminarily shaped into a 3D bulk form (BMOF) and was further combined with a thin lightweight Ni—Ni_3S_2 mesh using sodium carboxymethylcellulose (CMC-Na), resulting in a Ni—Ni_3S_2 mesh/BMOF hygrophotothermal hybrid. Remarkably, this hybrid retained a high water uptake of 0.6350 g g^{-1} even after interfacing the BMOF with the photothermal layer (dropped by only 28.6% compared to pristine BMOF), and impressive adsorption kinetics due to the penetrability of Ni—Ni_3S_2 mesh. In one sorption cycle, the hybrid with Ni—Ni_3S_2 mesh shows a high sorption kinetic of 3.18×10^{-3} g g^{-1} min^{-1}, higher than those with other Ni—Ni_3S_2 structures such as foil, granule, and foam, highlighting the effectiveness of this material design. It's worth noting that this is the first AWH design constructed by metal-semiconductor mesh and MOFs. Due to its structural characteristics (especially because of the Ni—Ni_3S_2 mesh), Ni—Ni_3S_2 mesh/BMOF hybrid exhibits unique and previously unreported features, such as high water uptake and absorption kinetics due to the penetrability of mesh structure, and high-efficiency and uniform desorption behavior due to the exterior photo-thermal Ni_3S_2 mesh and internal Ni with high thermal conductivity. This approach opens up new avenues for the efficient deployment of AWH in high-RH regions experiencing water scarcity, offering a fresh perspective on enhancing desorption kinetics by harnessing solar energy.

2. Results and Discussion

The synthesis of the hybrid Ni—Ni_3S_2 mesh/BMOF was conducted through a two-step process as detailed in **Figure 1a** and further elaborated in Section 1 (Supporting Information). First, Ni_3S_2 was in situ grown on the surface of a thermally conductive Ni mesh to form Ni—Ni_3S_2 mesh with superior photothermal

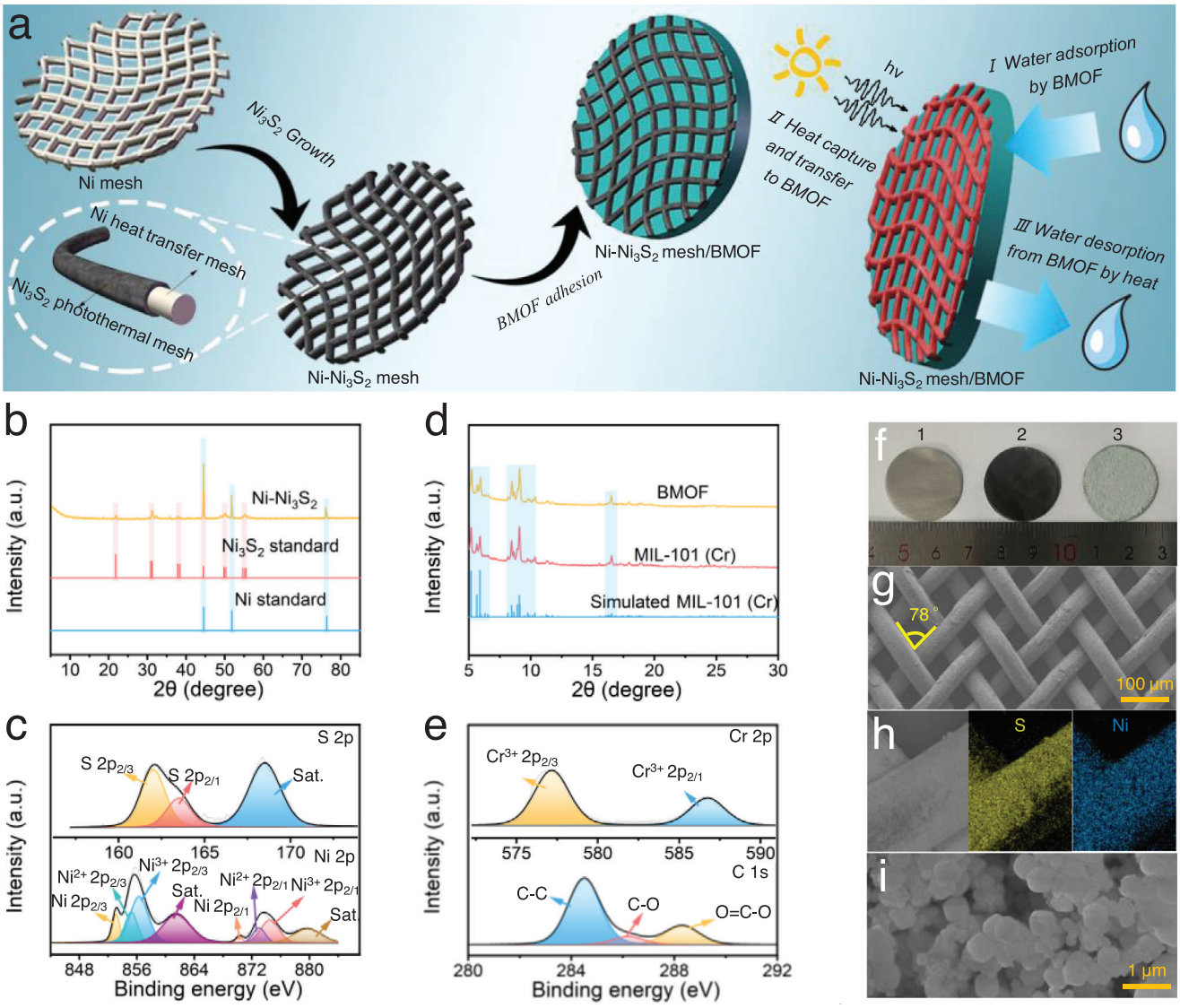

Figure 1. Synthesis of Ni—Ni_3S_2 mesh/BMOF a) Schematic illustration of Ni—Ni_3S_2 mesh/BMOF synthesis. b,d) XRD spectra of Ni—Ni_3S_2 (b), MIL-101 (Cr), and BMOF (d). c,e) XPS spectra of Ni—Ni_3S_2 mesh in S 2p and Ni 2p regions (c), and BMOF in Cr 2p and C 1s regions (e). f) Digital photographs of Ni mesh, Ni—Ni_3S_2 mesh, and Ni—Ni_3S_2 mesh/BMOF. g,h) SEM image of Ni—Ni_3S_2 mesh (g) and its corresponding EDS elemental mapping (h). i) SEM image of BMOF.

conversion and heat conduction properties. The Ni_3S_2 particles exhibited a strong mechanical adhesion to the Ni mesh (Figure S8, Supporting Information). Subsequently, the adhesive (CMC-Na), was utilized at an optimal concentration of 5% (Figure S9, Supporting Information) to convert powdery MOF into a bulk form (BMOF) and to adhere the BMOF onto one side of the Ni—Ni_3S_2 mesh, forming a hybrid photothermal adsorbent. In operation, BMOF adsorbs atmospheric moisture into its pores, while the Ni—Ni_3S_2 mesh captures sunlight, rapidly heating and transferring this photothermal energy to BMOF for efficient water desorption.

Analyses confirming the synthesis of the hybrid Ni—Ni_3S_2 mesh/BMOF are as follows. In the X-Ray Diffraction (XRD) spectrum of Ni—Ni_3S_2 in Figure 1b, peaks at 2θ = 21.8°, 31.1°, 31.8°, 37.8°, 38.4°, 44.5°, 49.8°, 50.2°, 54.7°, and 55.5° were the characteristic peaks of Ni_3S_2, corresponding to the (010), (110), (−110), (111), (−111), (020), (120), (−120), (112) and (−121) planes in the Ni_3S_2 standard (PDF#76-1870) respectively.[35] Peaks at 2θ = 44.5°, 52.4°, and 76.8° were the characteristic peaks of Ni, corresponding to the (111), (200), and (220) planes in the Ni standard (PDF#04-0850) respectively.[36] Figure 1c shows the X-ray photoelectron spectroscopy (XPS) spectra of Ni—Ni_3S_2 in S 2p and Ni 2p regions. In S 2p region, peaks at 162.0, 163.5, and 168.5 eV represented S $2p_{3/2}$, S $2p_{1/2}$, and the satellite peak of S respectively, while in Ni 2p region, peaks at 855.2, 856.3, 873.0, and 874.5 eV represented Ni^{2+} $2p_{3/2}$, Ni^{3+} $2p_{3/2}$, Ni^{2+} $2p_{1/2}$, and Ni^{3+} $2p_{1/2}$ respectively, indicating the growth of Ni_3S_2. Peaks at 853.0 and 870.3 eV were Ni $2p_{3/2}$ and Ni $2p_{1/2}$ respectively, confirming the existence of Ni.[36,37] Both XRD and XPS results confirmed the successful growth of Ni_3S_2 on the Ni mesh surface.

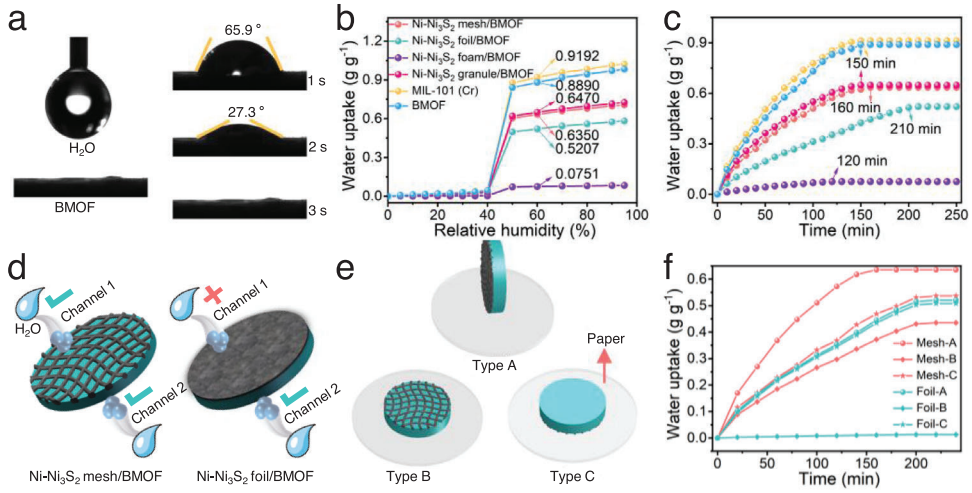

Figure 2. Water adsorption ability of Ni—Ni_3S_2 mesh/BMOF. a) Time-dependent contact angle to water of BMOF. b,c) Isothermal (b) and static water adsorption (c; 60%RH) curves of MIL-101 (Cr), BMOF, Ni—Ni_3S_2/BMOF with different Ni—Ni_3S_2 structures at 25 °C. d,e) Schematic illustration of water migration channels (d) and different adsorption types (e) of Ni—Ni_3S_2 mesh/BMOF and Ni—Ni_3S_2 foil/BMOF. f) Static water adsorption curves of Ni—Ni_3S_2 mesh/BMOF and Ni—Ni_3S_2 foil/BMOF with different adsorption types at 25 °C, 60% RH.

Figure 1d shows the XRD spectra of MIL-101 (Cr) and BMOF. Peak groups in the range within 5–6.5°, 8.1–10.3°, and 16.0–16.9° were the characteristic ones of MIL-101 (Cr), matching those in the simulated card (605 510[38]). BMOF had similar peaks compared to MIL-101 (Cr), without the obvious appearance of new peaks because of a small CMC-Na content. Figure 1e shows the XPS spectra of BMOF in the Cr 2p and C 1s regions. In the Cr 2p region, peaks at 577.6 and 587.0 eV represented Cr^{3+} $2p_{3/2}$ and Cr^{3+} $2p_{1/2}$ respectively. In the C 1s region, peaks at 284.7, 286.2, and 288.7 eV represented the C—C, C—O, and O═C—O respectively, showing the existence of the carboxylate group in BMOF (Figure S10, Supporting Information).[39,9] The details of the XPS analysis are shown in Figure S30 (Supporting Information).

Digital photographs of Ni mesh, Ni—Ni_3S_2 mesh, and Ni—Ni_3S_2 mesh/BMOF are shown in Figure 1f, marked with serial numbers 1, 2, and 3, respectively. Upon macroscopic examination, the Ni mesh underwent a noticeable transformation, losing its metallic luster and assuming a black hue, indicative of the formation of Ni—Ni_3S_2. Microscopic analysis, as presented in Figure 1g, revealed that the Ni—Ni_3S_2 mesh comprised intertwined Ni—Ni_3S_2 strips, maintaining a stack angle of 78°, identical to that of the original Ni mesh as shown in Figure S11a (Supporting Information). The width of Ni—Ni_3S_2 strips was ≈36 µm, slightly higher than that of Ni strip (≈31 µm) due to the growth of dense and wave-like stratiform Ni_3S_2 on Ni (Figure S11b–d, Supporting Information). This confirmed that the Ni mesh remained structurally intact in the core post-synthesis of Ni_3S_2, thereby preserving the expected heat conduction properties of the Ni mesh in terms of efficiency, continuity, and uniformity. Energy-dispersive X-ray spectroscopy (EDS) elemental mapping presented in Figure 1h highlighted the distribution of S and Ni elements, marked in yellow and blue respectively. This distribution closely followed the contours of the Ni—Ni_3S_2 strips. In the pristine Ni mesh, however, sulfur is evidently scant (Figure S12, Supporting Information). This confirmed the successful in situ formation and uniform distribution of Ni_3S_2 onto the Ni mesh. Figure 1i shows the scanning electron microscope (SEM) image of BMOF. The light globules are MOF crystals with a width of ≈0.2–0.3 µm. The smaller size of these particles contributed to a greater specific surface area and a higher number of sorption sites, significantly contributing to the adsorption capacity and kinetics of the hybrid Ni—Ni_3S_2 mesh/BMOF system.

Figure 2a shows the time-dependent contact angle of BMOF to water. At 1 and 2 s, the angles were respectively 65.9 and 27.3°, indicating the hydrophilicity of BMOF permitted by its hydrophilic groups and open metal sites. But more importantly, the sharp drop in the contact angle was caused by the high water adsorption capacity of BMOF, as evident from the near-zero contact angle at 3 s, indicating that the water is completely adsorbed into the abundant pores of BMOF and the voids between MOF crystals (Figure S13, Supporting Information). The average pore diameter ($R_{average}$) was relatively high (1.9605 nm), so MIL-101 (Cr) had difficulty desorbing water due to the irreversible capillary condensation in pores with large diameters (Table S1, Supporting Information).[40,41] Also, MIL-101 (Cr) had a high pore volume (V_{pore}) of 1.2014 cm^3 g^{-1}, which lowered the diffusion resistance of moisture and provided water cages during the adsorption, allowing MIL-101 (Cr) to have a high water uptake of 0.9192 g g^{-1} at 60% RH and 25 °C, as shown in Figure 2b. MIL-101 (Cr) exhibits a typical S-shaped isotherm, characterized by a low sorption plateau under 40% RH and a steep increase in water uptake above 40% RH. While this sorption behavior may not suit arid areas with RH below 30%, it makes MIL-101 (Cr) an ideal candidate for humid, water-scarce regions.[23] The incorporation of CMC-Na into BMOF marginally decreased its water uptake to 0.8890 g g^{-1}, a reduction of 3.3% from MIL-101 (Cr). This reduction was less significant than the proportion of CMC-Na added, attributable to its intrinsic water adsorption capability (Figure S14, Supporting Information). The BMOF layer thickness was set to 1.25 mm, balancing adsorption capacity considerations (Figure S15a, Supporting Information). Subsequently, the resultant Ni—Ni_3S_2 mesh/BMOF

exhibited a water uptake of 0.6350 g g^{-1}, marking a decrease of only ≈28.6% compared to the unmodified BMOF, benefiting from the incorporation of a lightweight Ni—Ni_3S_2 mesh (0.078 g). To comprehensively assess the sorption behavior of Ni—Ni_3S_2 mesh/BMOF, comparative analyses were conducted with various Ni—Ni_3S_2 configurations, including Ni—Ni_3S_2 foil/BMOF, Ni—Ni_3S_2 granule/BMOF, and Ni—Ni_3S_2 foam/BMOF. For the first three configurations (mesh, foil, granule), the masses of both the BMOFs and the Ni—Ni_3S_2 structures were standardized in Figure S15b (Supporting Information), and the digital photographs, schematic diagram of the preparation, SEM images, and EDS mappings of configurations are shown in Figures S1–S5,S37 (Supporting Information) respectively. The component masses in the Ni—Ni_3S_2 foam/BMOF were determined after optimization for ideal performance (Figure S15c, Supporting Information). At 60% RH and 25 °C, the water uptakes for the Ni—Ni_3S_2 foil/BMOF, Ni—Ni_3S_2 granule/BMOF, and Ni—Ni_3S_2 foam/BMOF were 0.5207, 0.6470, and 0.0751 g g^{-1}, respectively. The presence of Ni—Ni_3S_2 which has a certain weight but no sorption capacity inevitably reduced the water uptake of the hybrid photothermal sorbent (Figure S16, Supporting Information). Consequently, Ni—Ni_3S_2 foam/BMOF, bearing a heavier Ni—Ni_3S_2 framework exhibits a poorer water uptake on a per-gram basis. Comparatively, Ni—Ni_3S_2 mesh/BMOF and Ni—Ni_3S_2 granule/BMOF exhibit similar water capacities, whereas Ni—Ni_3S_2 foil/BMOF demonstrates a notably lower capacity. This reduction can be attributed to the existence of an inert BMOF layer adjacent to the Ni—Ni_3S_2 foil (Figure S17, Supporting Information). In Figure 2c, MIL-101 (Cr), BMOF, and Ni—Ni_3S_2 granule/BMOF reached adsorption saturation in 150 min, while Ni—Ni_3S_2 mesh/BMOF, Ni—Ni_3S_2 foil/BMOF, Ni—Ni_3S_2 foam/BMOF reached adsorption saturation in 160, 200, and 125 min, respectively. The integration of CMC-Na and Ni—Ni_3S_2 granules did not significantly alter the water isotherm trends of the sorbents. The Ni—Ni_3S_2 foam structure, providing an enhanced contact area for BMOF, facilitated more efficient moisture transfer, resulting in the shortest saturation time among the configurations tested. The adsorption saturation time for Ni—Ni_3S_2 foil/BMOF increased by 60 min compared to pristine BMOF, while for Ni—Ni_3S_2 mesh/BMOF, it extended merely by 10 min in relation to pristine BMOF.

Considering the observed variation in adsorption kinetics across different configurations, a hypothesis was formulated as illustrated in Figure 2d. In the Ni—Ni_3S_2 mesh/BMOF configuration, moisture is theorized to migrate through both Channel 1 and Channel 2 toward BMOF. The large openings in Ni—Ni_3S_2 mesh with penetrability provide an easy path for water to reach the underlying BMOF. In contrast, the Ni—Ni_3S_2 foil/BMOF configuration restricts moisture migration solely to Channel 2 leading directly to BMOF. During the adsorption process, the MOF layer, possessing a specific thickness, encounters inherent resistance to both mass and heat transfer.[42] This resistance increasingly impedes the adsorption of water vapor into the deeper layers of the MOF, a phenomenon observed across all configurations. The design effectively acts to reduce the functional thickness of the BMOF layer, thereby enhancing sorption kinetics in comparison to a system permitting only one-sided sorption, accounting for the observed differences in adsorption rates between configurations and supports the notion that the presence of an inert layer in the Ni—Ni_3S_2 foil/BMOF configuration restricts its adsorption capacity.

To test this hypothesis, a simple experiment was carried out (depicted in Figure 2e), utilizing a flat, non-breathable paper to obstruct either the Ni—Ni_3S_2 (foil or mesh) or BMOF sides, termed Type B and Type C adsorption, respectively, contrasted against Type A, which had no adsorption restrictions. For Ni—Ni_3S_2 foil/BMOF, adsorption curves of Type A and Type C were similar, but Type B showed poor adsorption behavior, demonstrating that only the BMOF side in Ni—Ni_3S_2 foil/BMOF offered sorption channels (Figure 2f). In Ni—Ni_3S_2 mesh/BMOF, we observed a distinct trend in adsorption performance, with Type A adsorption demonstrating the highest kinetics and capacity, followed by Type C, and Type B presenting the lowest. This trend not only confirms the contribution of both the BMOF and Ni—Ni_3S_2 mesh sides to the adsorption process but also highlights the dominant role of the BMOF channel. The reduced performance in Type B adsorption can be attributed to the Ni—Ni_3S_2 mesh acting partially as a barrier to sorption, thus limiting the overall adsorption capacity. These results validated the hypothesis, showing that the Ni—Ni_3S_2 mesh/BMOF, with its perforated open-structured design, offers high water sorption kinetics and capacity.

Solar-driven desorption, a prominent method for releasing trapped water without additional energy input, often faces challenges in achieving rapid and complete desorption due to insufficient solar-to-thermal energy conversion and ineffective and non-uniform heat transfer.

The desorption activation energy (E_d) of sorbents is calculated based on Equation (1):[43]

$$\ln\left(\frac{\beta}{RT_d^2}\right) = -\left(\frac{E_d}{RT_d}\right) - \ln\left(\frac{E_d}{k_0}\right) \quad (1)$$

In this equation, R is the gas constant (8.315 J mol^{-1} K^{-1}), β is the heating rate (K min^{-1}), and T_d is the temperature (K) at the peak desorption rate (Table S2, Figure S18, Supporting Information). Based on this equation, the E_d for MIL-101 (Cr) and BMOF were fitted and calculated to be 42.16 and 41.43 kJ mol^{-1}, respectively (**Figure 3a**). The open metal sites of MOFs cause a strong binding force to the water molecules during the adsorption process, necessitating high E_d for the desorption process. Moreover, the capillary condensation in MIL-101 (Cr) and BMOF with high $R_{average}$ was significant, increasing the energy required for desorption (Table S1, Supporting Information). At lower temperatures, the MOF struggles to break the bonds between water molecules and the open metal sites, leading to a slow and incomplete desorption process (Figure S19, Supporting Information). Conversely, the remarkable solar absorption capability of Ni_3S_2 and the compact structure of BMOF significantly enhance photothermal conversion and heat transfer, respectively (Figures S20,S21, Supporting Information).

In Figure 3b, under 1 kW m^{-2} and 25 °C, pre-adsorbed MIL-101 (Cr) and BMOF both showed similar modest temperature rise to ≈44 °C in 30 min, affecting the speed and depth of desorption. Contrastingly, configurations incorporating Ni—Ni_3S_2, namely Ni—Ni_3S_2 mesh/BMOF, Ni—Ni_3S_2 foil/BMOF, Ni—Ni_3S_2 foam/BMOF, and Ni—Ni_3S_2 granule/BMOF witnessed

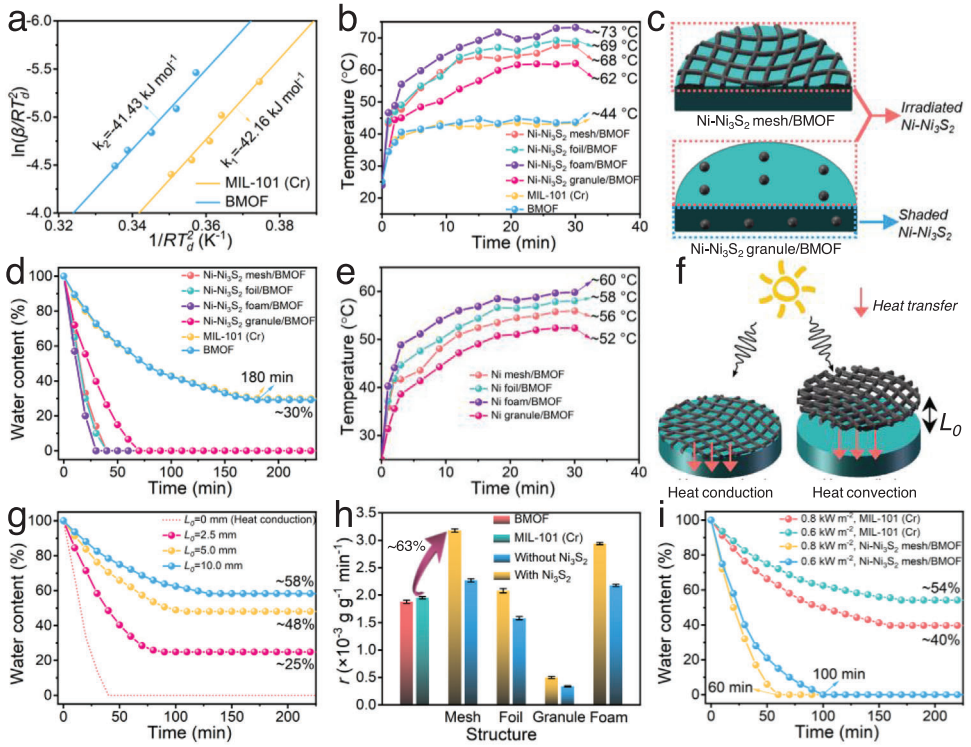

Figure 3. Water desorption ability of Ni—Ni_3S_2 mesh/BMOF. a) Linear fitting for the desorption activation energy of MIL-101 (Cr) and BMOF. b,d) Photothermal heating (b) and desorption (d) curves of MIL-101 (Cr), BMOF, and Ni—Ni_3S_2/BMOF with different Ni—Ni_3S_2 configurations at 25 °C and 1.0 kW m^{-2}. c) Schematic illustration of irradiated and shaded Ni—Ni_3S_2 in Ni—Ni_3S_2 mesh/BMOF and Ni—Ni_3S_2 granule/BMOF. e) Heating curves of Ni/BMOF with different Ni structures at 25 °C and 1.0 kW m^{-2}. f) Schematic illustration of heat conduction in Ni—Ni_3S_2/BMOF and heat convection from Ni—Ni_3S_2 to BMOF. g) Desorption curves of BMOF at 25 °C and 1.0 kW m^{-2} when L_0 were 2.5, 5.0, and 10.0 mm. h) Bar graph of the sorption rates of MIL-101 (Cr) and BMOF, as well as Ni—Ni_3S_2/BMOF and Ni/BMOF with different structures. i) Desorption curves of MIL-101 (Cr) and Ni—Ni_3S_2 mesh/BMOF at 25 °C (0.6 and 0.8 kW m^{-2}).

temperature elevations to ≈68, ≈69, ≈73, and ≈62 °C, respectively. Among these, Ni—Ni_3S_2 foam/BMOF demonstrated the greatest thermal efficiency due to its higher content of Ni—Ni_3S_2, yet it displayed the least effective water adsorption capacity. Both Ni—Ni_3S_2 mesh/BMOF and foil/BMOF exhibited similar thermal responses, surpassing that of the granule/BMOF variant. In the mesh variant (Figure 3c), a larger area of Ni—Ni_3S_2 is exposed to irradiation compared to the granule variant, where significant shading of Ni—Ni_3S_2 granules at the core or base reduces the effective absorption area. The mesh configuration is therefore more efficient in promoting desorption by allowing greater light absorption and heat distribution. In Figure 3d, pre-adsorbed (60% RH and 25 °C) sorbents were irradiated under 1 kW m^{-2}. Ni—Ni_3S_2 mesh/BMOF, Ni—Ni_3S_2 foil/BMOF, Ni—Ni_3S_2 foam/BMOF, and Ni—Ni_3S_2 granule/BMOF desorbed trapped water completely in 40, 40, 30, and 70 min, respectively, while BMOF and MIL-101 (Cr) cannot completely desorb water and reached sorption equilibrium at 180 min with ≈30% residual water. These residual water molecules were very difficult to desorb due to the poor light absorbance of sorbents and high binding energy.

Some comparative experiments were conducted to further analyze the desorption mechanism. First, all Ni—Ni_3S_2 structures were replaced by Ni structures. In Figure 3e, under 1 kW m^{-2} and 25 °C, pre-adsorbed Ni mesh/BMOF, Ni foil/BMOF, Ni foam/BMOF, and Ni granule/BMOF heated to ≈56, ≈58, ≈60, and ≈52 °C in 30 min, lower by ≈12, ≈11, ≈10, and 13 °C compared to those with Ni_3S_2, respectively, proving the better light absorbance of Ni—Ni_3S_2 (Figure S21, Supporting Information). It's worth noting that the growth of Ni_3S_2 on Ni caused negligible increases in mass (less than 2%) irrespective of the configuration (Figure S22, Supporting Information), benefitting the gravimetric water uptake performance of the hybrid sorbent. Predictably, due to lower temperature rise, Ni/BMOFs had poorer solar-driven desorption ability than Ni—Ni_3S_2/BMOFs with the same configuration, which is evident from the longer time durations required for complete desorption (Figure S23, Supporting Information).

Furthermore, the mode of heat transfer also greatly affected the desorption, as shown in Figure 3f. Heat transfer between the Ni—Ni_3S_2 mesh and BMOF predominantly occurs through conduction, thanks to their direct contact which enables rapid and substantial heat exchange. To validate this mechanism, the Ni—Ni_3S_2 mesh and BMOF were deliberately separated by varying distances (L_0), transitioning the mode of heat transfer from conduction to convection, and the experimental detail is shown in Figure S24 (Supporting Information).

As can be seen in Figure 3g, an increase in L_0 resulted in a noticeable decline in the desorption rate of BMOF. Specifically, with L_0 set at 2.5, 5.0, and 10.0 mm, the proportion of water

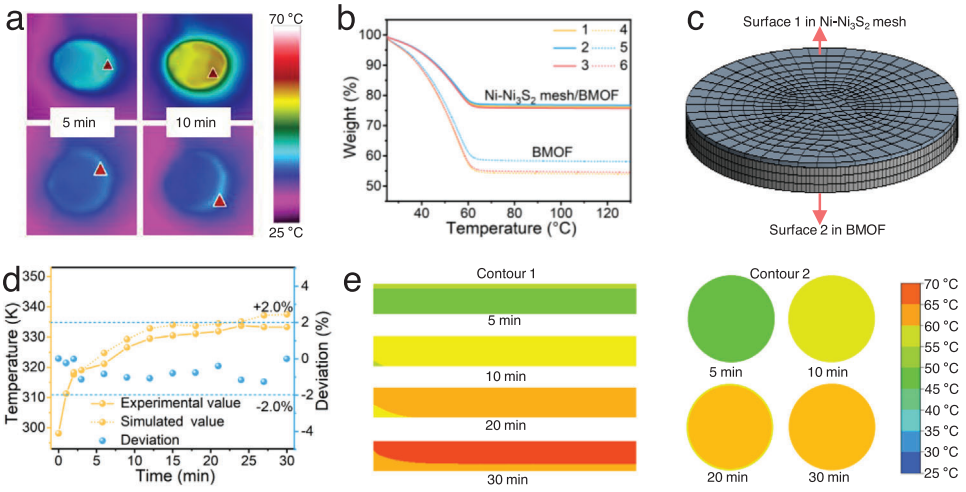

Figure 4. Heat transfer simulation of Ni—Ni_3S_2 mesh/BMOF. a) Infrared thermal images of Ni—Ni_3S_2 mesh/BMOF (upper) and MIL-101 (Cr) (lower) at 25 °C and 1.0 kW m^{-2}. b) TG curves of BMOF and Ni—Ni_3S_2 mesh/BMOF. c) Schematic diagram of the meshed model of Ni—Ni_3S_2 mesh/BMOF. d) Experimental and simulated temperature curves of Surface 2 in Ni—Ni_3S_2 mesh/BMOF and their deviations. e) Simulated temperature cloud maps of Contour 1 and Contour 2 in Ni—Ni_3S_2 mesh/BMOF.

remaining post-desorption was ≈25%, 48%, and 58%, respectively, indicating a reduced heat transfer efficiency. These findings underscore the crucial role of the direct contact between Ni—Ni_3S_2 and BMOF in ensuring efficient heat transfer and thereby facilitating optimal desorption. In the absence of such direct contact, the substantial heat generated by the Ni—Ni_3S_2 cannot be effectively transferred to the sorbent, leading to suboptimal desorption outcomes. In Figure 3h, the overall sorption rate (r) of sorbents was calculated by Equation (2), based on the adsorption and desorption rates (Table S3, Supporting Information).

$$r = \frac{aw}{t} \tag{2}$$

In Equation (2), a is the desorption completion ratio of the sorbent (i.e., a is 100% for complete desorption). t is the total time to complete one cycle, including adsorption time (t_a) at 25 °C, 60% RH, and desorption time at 1.0 kW m^{-2} (t_d). When sorbents cannot reach complete desorption, t_d is the time at the onset of saturation when the desorption curve begins to plateau. w is the water uptake of the sorbent at 60% RH and 25 °C. This formula revealed that the overall sorption rates of BMOF and MIL-101 (Cr) were closely matched, at 1.89×10^{-3} and 1.95×10^{-3} g g^{-1} min^{-1}, respectively. r of Ni—Ni_3S_2 mesh/BMOF, Ni—Ni_3S_2 foil/BMOF, Ni—Ni_3S_2 foam/BMOF and Ni—Ni_3S_2 granule/BMOF were 3.18×10^{-3}, 2.08×10^{-3}, 0.5×10^{-3}, and 2.94×10^{-3} g g^{-1} min^{-1}, enhanced by 40.01%, 44.30%, 47.06%, and 35.48% compared to those without Ni_3S_2, respectively (Table S3, Supporting Information). r of MIL-101 (Cr) enhanced by ≈63% after assembling with Ni—Ni_3S_2 mesh, boosting the potential water yield.

Additionally, under reduced irradiance (0.6 and 0.8 kW m^{-2}), pre-adsorbed Ni—Ni_3S_2 mesh/BMOF displayed shorter desorption times (100 and 60 min, respectively) compared to MIL-101 (Cr), which was unable to fully desorb water, leaving ≈54% and ≈40% residual water in 180 mins, respectively. Under 0.6, 0.8 kW m^{-2}, r of Ni—Ni_3S_2 mesh/BMOF enhanced by 90.62% and 73.05%, respectively. This performance indicates a pronounced improvement in desorption kinetics under lower light conditions, suggesting that Ni—Ni_3S_2 mesh/BMOF could offer considerable advantages in regions with less sunlight. Overall, these results affirm the enhanced water yield capabilities of Ni—Ni_3S_2 mesh/BMOF, despite a minor trade-off in sorbent's adsorption capacity and kinetics, thereby expanding the potential application spectrum for sorbents in various environmental settings.

In **Figure 4a**, the Ni—Ni_3S_2 mesh/BMOF demonstrates a rapid and significant thermal response upon exposure to light, setting it distinctly apart from the ambient temperature profile. Red triangles within the profiles of Ni—Ni_3S_2 mesh/BMOF mark the points of highest temperature observed in infrared imagery. This temperature distribution across the Ni—Ni_3S_2 mesh/BMOF appears uniform, characterized by circular outlines of consistent color, indicative of homogenous heat distribution. The cyan and blue regions, expanding over time along the periphery of the circular temperature profile indicate the heat exchange between Ni—Ni_3S_2 mesh/BMOF and its environment. This exchange is notably more pronounced than that observed with MIL-101 (Cr), evidenced by a greater temperature differential between Ni—Ni_3S_2 mesh/BMOF and its surroundings. In contrast, MIL-101 (Cr) displays a light blue crescent ring in its temperature profile, indicating variations in internal temperature. Such differences suggest that the desorption behavior of sorbents across various zones may vary due to uneven heat transfer, leading to non-uniform mass transfer rates. Consequently, this disparity can extend the desorption duration, particularly when tackling the release of residual water molecules that are more challenging to desorb. This phenomenon underscores the importance of achieving a uniform thermal response to facilitate efficient and synchronous desorption across the entire sorbent material.

Under 1.0 kW m^{-2} illumination for 20 minutes, the desorption behavior at different points within adsorption-saturated (60% RH

and 25 °C) Ni—Ni_3S_2 mesh/BMOF and MIL-101 (Cr) was investigated. It's worth noting that the two sorbents still had residual water since the water could not be desorbed completely in 20 mins (Figure 3d). These points were designated as Points 1–3 for Ni—Ni_3S_2 mesh/BMOF and Points 4–6 for BMOF, with further details provided in the Supporting Information (Figure S25, Supporting Information). In Figure 4b, thermogravimetric (TG) analysis revealed that the desorption curves for Points 1–3 in Ni—Ni_3S_2 mesh/BMOF exhibited similarity, indicating consistent desorption across these points. Conversely, the curves for Points 4–6 in BMOF showed significant variation, highlighting discrepancies in desorption uniformity. Specifically, desorption at Point 6 in BMOF was prolonged compared to Point 5, likely due to greater heat dissipation to the surroundings at the material's edge.

The homogeneity of mass transfer is closely linked to the temperature distribution within the sorbent. To visualize this distribution, the simulation software Fluent was utilized, focusing on the sun-illuminated temperature profile of Ni—Ni_3S_2 mesh/BMOF. Detailed information about the mathematical modeling employed is available in Section 19 (Supporting Information). In Figure 4c, the simulation model, accurately reflecting the real dimensions (Figure S26, Supporting Information), was segmented into upper Ni—Ni_3S_2 and lower BMOF sections. Prior to the simulation, temperatures at the illuminated surface (Surface 1) and the underside of Ni—Ni_3S_2 mesh/BMOF (Surface 2) were experimentally determined. In the simulation depicted in Figure 4d, the temperature at Surface 1 was input as the experimentally measured value, whereas the temperature at Surface 2 was derived from the simulation for comparative analysis. The experimental and simulated temperature curves of Surface 2 had a similar trend. The deviation (σ) from the experimental value was lower than 2.0% (mostly within 1.5%) based on Equation (3):

$$\sigma = \left(\frac{T_S - T_E}{T_E}\right) \tag{3}$$

here, T_S and T_E represent the simulated and experimental temperatures (in Kelvin), respectively. The minor deviation (σ) and the demonstrated grid independence (Figure S27, Supporting Information) attest to the model's reliability. Based on this validation, two contours within the model were defined to check the temperature distribution across the Ni—Ni_3S_2 mesh/BMOF (depicted in Figure S28, Supporting Information). Contour 1 represents the half-section of the geometric center in the Z–Y plane through the Ni—Ni_3S_2 and BMOF layers, whereas Contour 2 corresponds to Surface 2 in the X–Y plane. The temperature cloud maps shown in Figure 4e reveal that temperatures in both contours rose over time, displaying minimal variation, with the presence of up to two adjacent colors on the temperature axis. This observation confirms slight temperature differentials across various zones of Ni—Ni_3S_2 mesh/BMOF at all measured time intervals.

In Contour 1, temperature deviations primarily arose from two factors. Initially, at the 5-min mark, a minimal temperature differential between the Ni—Ni_3S_2 mesh and BMOF was noted, attributable to low thermal resistance at their adjoining interfaces. Subsequently, from 5 to 30 min, significant heat exchange with the environment through natural convection, particularly at the lower left of BMOF, led to increasing temperature deviations, reaching peak deviation at 30 min. This trend underscores the maximal heat loss to the surroundings during this period. Meanwhile, temperature variation within Contour 2 was found to be negligible.

These findings highlight the uniform temperature distribution across the X–Y and Z–Y planes of the integrated Ni—Ni_3S_2 mesh/BMOF system. The large heating surface area of the Ni—Ni_3S_2, coupled with its internal thermally conductive Ni framework, ensures temperature uniformity in the X–Y plane. Conversely, the relatively thin BMOF layer and the minimal air gap (filled with CMC-Na) preventing high thermal resistance between MOF crystals, enhance temperature uniformity in the Z–Y plane. These structural attributes enable efficient and uniform transfer of photogenerated heat from the Ni—Ni_3S_2 mesh to BMOF, facilitating rapid and homogeneous water desorption.

Therefore, the mechanism can be summarized into two steps based on all the above-mentioned results. First, Ni—Ni_3S_2 mesh/BMOF maintained excellent adsorption due to the penetrability of the Ni—Ni_3S_2 mesh. This conclusion was obtained based on the contrasting adsorption behavior characterizations, as shown in Figure 2d–f. Second, under illumination, Ni—Ni_3S_2 mesh can heat up quickly due to good photothermal conversion and large irradiation area, and the photo-generated heat was efficiently and uniformly transferred to BMOF to promote swift desorption. This was proved by the designed contrasting desorption kinetics characterizations (Figure 3b–g) and the computational simulations (Figure 4e).

Furthermore, a water-generation experiment under closed conditions was carried out, demonstrating the enhanced performance of Ni—Ni_3S_2 mesh/BMOF, as shown in Figure S29 (Supporting Information). **Figure** 5a depicts the cyclic water adsorption–desorption behavior of Ni—Ni_3S_2 mesh/BMOF. Each cycle consisted of a water adsorption phase at 25 °C and 60% RH for 150 min, followed by a desorption phase at 25 °C under 1 kW m^{-2} irradiation for 40 mins. The dotted lines mark the water uptake levels in Ni—Ni_3S_2 mesh/BMOF post-adsorption and post-desorption, and the specific water uptakes are shown in Table S5 (Supporting Information). Notably, after 50 cycles, there was minimal fluctuation in performance, indicating high cyclic stability.

This stability can be attributed to several factors. First, MIL-101 (Cr) with inert metal clusters is reported to have good thermal stability due to kinetic inertia under high temperatures, and good hydrothermal stability.[44,45] Second, the temperature increase under solar illumination is sufficient for effective water desorption but remains below the threshold that might induce chemical reactions of Ni_3S_2 in the air. The structural integrity of Ni_3S_2, including its wave-like stratiform architecture, elemental composition, and crystalline structure on the Ni mesh, remained consistent before and after cycling (Figures S30,S31, Supporting Information).

Besides the excellent cycling performance stability, the morphological stability was also evaluated. Illustrated in Figure 5b is a chamber at 25 °C and 60% RH with a fan to generate a moist airflow. MIL-101 (Cr) powder was spread flat on the paper, while other sorbents were vertically positioned (designated as Type A in Figure 2e). When subjected to this airflow, in just 10 min, all lightweight MIL-101 (Cr) powders got dispersed by the airflow

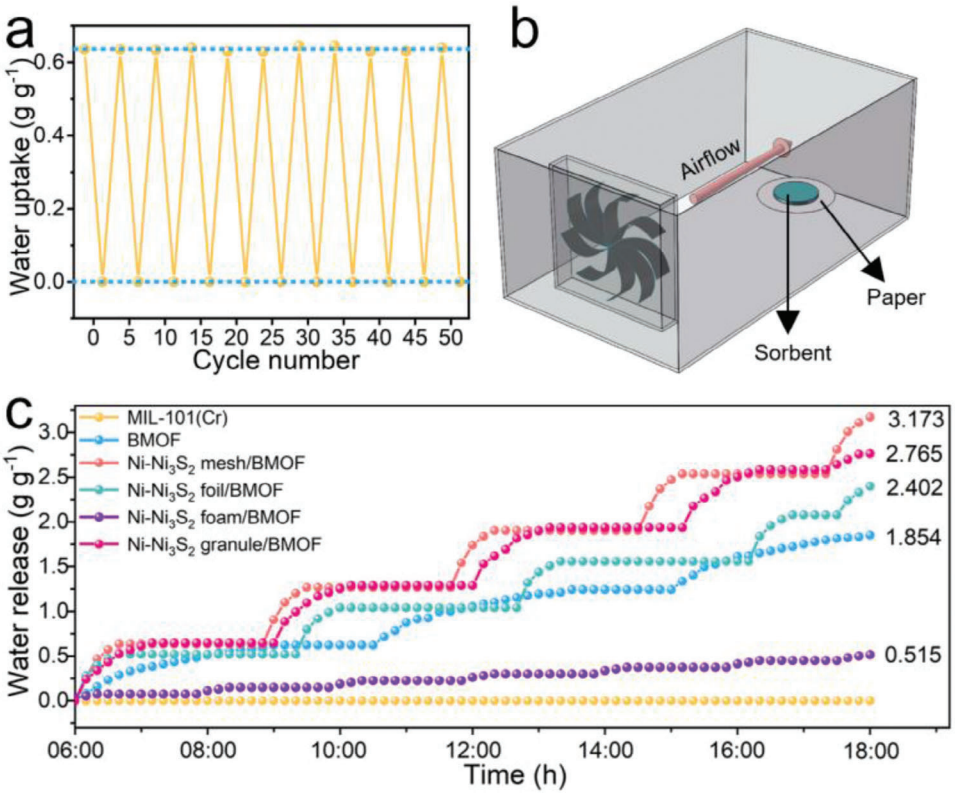

Figure 5. Stability of Ni—Ni_3S_2 mesh/BMOF. a) Cyclic dynamic water adsorption–desorption curve of Ni—Ni_3S_2 mesh/BMOF. b) Schematic diagram of the chamber with airflow. c) Daily water release curves of sorbents at 25 °C and 60%RH.

which could cause potential issues such as sorbent loss and blockage in the water generator. The addition of CMC-Na enhanced the adhesion among MIL-101 (Cr) crystals through intermolecular forces, preventing undesirable dispersions under airflow. Consequently, MIL-101 (Cr) without CMC-Na showed a reduction to 0% of its initial mass after one complete sorption cycle, while the masses of other sorbents remained unchanged (Figure S32, Supporting Information), demonstrating their remarkable structural stability. The introduction of airflow significantly accelerated the adsorption kinetics (Figure S33, Supporting Information), reducing the saturation time for Ni—Ni_3S_2 mesh/BMOF, Ni—Ni_3S_2 foil/BMOF, Ni—Ni_3S_2 granule/BMOF, Ni—Ni_3S_2 foam/BMOF, and BMOF to 130, 160, 120, 90, and 110 min respectively (as opposed to 30, 50, 30, 30, and 40 min obtained without the airflow (Figure 2c), respectively) because of the enhanced mass transfer facilitated by the airflow. These findings underscore the importance of structural stability in the presence of natural convection and airflow.

In Figure 5c, the daily water release capacity of various sorbents was assessed within a chamber where the measured values might represent a limit due to the desorption process being executed under a specific condition of 1 kW m^{-2}. Each sorbent underwent water adsorption before 06:00 Hrs to achieve saturation and then proceeded with sorption cycles until 18:00 Hrs. The plateaus in the curves represent the adsorption process. Water release rates achieved by Ni—Ni_3S_2 mesh/BMOF, Ni—Ni_3S_2 foil/BMOF, Ni—Ni_3S_2 granule/BMOF, Ni—Ni_3S_2 foam/BMOF, and BMOF were 3.173, 2.402, 2.765, 0.515, and 1.854 g g^{-1} day^{-1}. Except for the Ni—Ni_3S_2 foam/BMOF configuration, all the other Ni—Ni_3S_2/BMOFs outperformed pristine BMOF, validating the effectiveness of the Ni—Ni_3S_2 mesh photothermal bridge in enhancing sorption dynamics. Specifically, water release from Ni—Ni_3S_2 mesh/BMOF surpassed that of BMOF by 71.14%, a figure closely aligned with the enhancement in sorption kinetics seen in Figure 3h. Furthermore, replacing MIL-101 (Cr) with some other conventional MOFs more suited to lower RH environments, such as Al-Fum, MOF-303, and MOF-801 (Figures S6,S7, Supporting Information), continued to demonstrate significant sorption rate enhancements over pristine MOFs (Figures S34–S36, Table S6, Supporting Information).[27,46,47] This underscores the broad applicability and efficacy of the Ni—Ni_3S_2 mesh photothermal bridge across various MOFs and the relevance of this design for future sorbent-based atmospheric water generation. This highlights the wide-ranging utility and effectiveness of the Ni—Ni_3S_2 mesh as a photothermal bridge in enhancing the AWH performance of diverse MOFs. The demonstration of this design approach signifies its potential impact on advancing sorbent technologies for humidity harvesting, underscoring its importance for future developments in the field.

3. Conclusion

In this study, we synthesized a Ni—Ni_3S_2 mesh/BMOF hybrid sorbent that integrates a photothermal Ni—Ni_3S_2 mesh with hygroscopic MOFs to enhance MOF desorption kinetics. This sorbent achieved adsorption saturation within 150 min at 60% RH

and 25 °C, demonstrating a water uptake of 0.6350 g g^{-1}. Despite the introduction of the Ni—Ni_3S_2 mesh, compared to pristine BMOF, the decrease in water uptake was limited to 28.6%, and the adsorption saturation time was extended merely by 10 min thanks to the penetrability of Ni—Ni_3S_2 mesh. The effective light absorbance, photothermal conversion, and uniform heat distribution and transfer facilitated by the Ni—Ni_3S_2 mesh established it as a photothermal bridge, enabling rapid heating to 68 °C under 1.0 kW m^{-2} and complete desorption in just 40 minutes—a capability not achievable with unmodified MIL-101 (Cr) alone. Notably, even under reduced sunlight conditions (0.6 and 0.8 kW m^{-2}), the sorbent exhibited modest desorption times of 100 and 60 min, respectively. The sorption kinetics of this hybrid sorbent, at 3.18×10^{-3} g g^{-1} min^{-1}, surpassed those of other Ni—Ni_3S_2 configurations (foil, granule, and foam), highlighting the effectiveness of the mesh design. Heat-transfer simulations confirmed the uniform thermal distribution across the Ni—Ni_3S_2 mesh/BMOF and elucidated the mechanism for rapid and uniform desorption. Additionally, through 50 cycles of adsorption–desorption, Ni—Ni_3S_2 mesh/BMOF exhibited minimal performance fluctuation, indicating considerable hydrothermal stability and long-term viability. Overall, our findings reveal that Ni—Ni_3S_2 mesh/BMOF presents optimized sorption behavior, robust cyclic stability, and efficient, rapid, and uniform desorption without the need for external/non-ambient energy input, marking it as a promising solution for atmospheric water harvesting in water-scarce regions with high relative humidity.

[605 510 contains the supplementary crystallographic data for this paper. The data can be obtained free of charge from The Cambridge Crystallographic Data Centre via www.ccdc.cam.ac.uk/data_request/cif.]

Supporting Information

Supporting Information is available from the Wiley Online Library or from the author.

Acknowledgements

The authors thank Zhen Zeng for his help in collecting the part of experimental data. This work was supported by the National Natural Science Foundation of China (Grant No. 51536003), Guangdong Provincial Foundation for Basic and Applied Basic Research (2022A1515110317), the innovatingIIproject of the University of Hong Kong (Grant No. 207300392), and City University of Hong Kong (Grant No. 7020100).

Conflict of Interest

The authors declare no conflict of interest.

Data Availability Statement

Research data are not shared.

Keywords

atmospheric water harvesting, heat transfer simulations, MIL-101 (Cr), photothermal conversion, solar-trigger desorption

Received: June 23, 2024
Revised: August 21, 2024
Published online: September 12, 2024

[1] Y. D. Tu, R. Z. Wang, Y. N. Zhang, J. Y. Wang, *Joule* **2018**, *2*, 1452.
[2] M. M. Mekonnen, A. Y. Hoekstra, *Sci. Adv.* **2016**, *2*, e1500323.
[3] Y. Song, M. Y. Zeng, X. Y. Wang, P. R. Shi, M. F. Fei, J. Zhu, *Adv. Mater.* **2023**, *36*, 12.
[4] M. Elimelech, W. A. Phillip, *Science* **2011**, *333*, 712.
[5] D. Zhang, J. H. Dai, M. J. Liang, M. X. Han, Q. Y. He, F. M. Chen, L. J. Li, *ACS Energy Lett.* **2023**, *8*, 2325.
[6] Z. X. Wang, J. Gao, J. J. Zhou, J. W. Gong, L. W. Shang, H. B. Ye, F. He, S. Q. Peng, Z. X. Lin, Y. X. Li, F. Caruso, *Adv. Mater.* **2023**, *35*, 135.
[7] H. Park, J. Kamcev, L. Robeson, M. Elimelech, B. Freeman, *Science.* **2017**, *356*, eaab0530.
[8] T. X. Li, M. Q. Wu, J. X. Xu, R. X. Du, T. S. Yan, P. F. Wang, Z. Y. Bai, R. Z. Wang, S. Q. Wang, *Nat. Commun.* **2022**, *13*, 6771.
[9] C. X. Lu, Y. Z. Zhou, L. Z. Li, H. W. Chen, L. S. Yan, *Fuel* **2023**, *333*, 126415.
[10] W. Shi, W. X. Guan, C. X. Lei, G. H. Yu, *Angew. Chem. Int. Ed.* **2022**, *61*, e202211267.
[11] S. Zhang, J. R. Fu, S. Das, K. Q. Ye, W. D. Zhu, T. Ben, *Angew. Chem. Int. Ed.* **2022**, *61*, e202208660.
[12] M. Ejeian, R. Z. Wang, *Joule* **2021**, *5*, 1678.
[13] F. Fathieh, M. J. Kalmutzki, E. A. Kapustin, P. J. Waller, J. Yang, O. M. Yaghi, *Sci. Adv.* **2018**, *4*, eaat3198.
[14] N. Hanikel, M. S. Prévot, O. M. Yaghi, *Nat. Nanotechnol.* **2020**, *15*, 348.
[15] W. Song, Z. Zheng, A. H. Alawadhi, O. M. Yaghi, *npj Clean Water* **2023**, *1*, 626.
[16] Z. L. Zheng, N. Hanikel, H. Lyu, O. M. Yaghi, *J. Am. Chem. Soc.* **2022**, *144*, 22669.
[17] N. Hanikel, X. K. Pei, S. Chheda, H. Lyu, W. Jeong, J. Sauer, L. Gagliardi, O. M. Yaghi, *Science* **2021**, *374*, 454.
[18] H. Kim, S. R. Rao, E. A. Kapustin, L. Zhao, S. Yang, O. M. Yaghi, E. N. Wang, *Nat. Commun.* **2018**, *9*, 1191.
[19] H. Kim, S. Yang, S. R. Rao, S. Narayanan, E. A. Kapustin, H. Furukawa, A. S. Umans, O. M. Yaghi, E. N. Wang, *Science* **2017**, *356*, 430.
[20] N. Hanikel, M. S. Prévot, F. Fathieh, E. A. Kapustin, H. Lyu, H. Wang, N. J. Diercks, T. G. Glover, O. M. Yaghi, *ACS Cent. Sci.* **2019**, *5*, 1699.
[21] F. Jeremias, A. Khutia, S. K. Henninger, C. Janiak, *J. Mater. Chem.* **2012**, *22*, 10148.
[22] M. P. Silva, A. M. Ribeiro, C. G. Silva, K. H. Cho, U. H. Lee, J. L. Faria, J. M. Loureiro, J. S. Chang, A. E. Rodrigues, A. Ferreira, *Sep. Purif. Technol.* **2022**, *290*, 120803.
[23] Y. Feng, T. Ge, B. Chen, G. Zhan, R. Wang, *Cell Rep. Phys. Sci.* **2021**, *2*, 9.
[24] H. S. Qi, T. Q. Wei, W. Zhao, B. Zhu, G. L. Liu, P. P. Wang, Z. H. Lin, X. Y. Wang, X. Q. Li, X. W. Zhang, J. Zhu, *Adv. Mater.* **2019**, *31*, 1903378.
[25] C. Y. He, Y. Li, Z. H. Zhou, B. H. Liu, X. H. Gao, *Adv. Mater.* **2024**, *36*, 24.
[26] Y. L. Tao, Q. Q. Li, Q. N. Wu, H. Q. Li, *Mater. Horiz.* **2021**, *8*, 1439.
[27] Y. X. Tan, W. C. Chen, Y. T. Fang, S. F. Wang, *Chem. Eng. J.* **2023**, *475*, 146353.
[28] W. C. Chen, Y. X. Liu, B. L. Xu, M. Ganesan, B. Q. Tan, Y. X. Tan, F. Luo, X. H. Liang, S. F. Wang, X. N. Gao, Z. G. Zhang, R. Q. Ye, D. Y. C. Leung, S. K. Ravi, Y. T. Fang, *Small* **2024**, *20*, 20.
[29] Y. Hu, Z. Fang, X. Wan, X. Ma, S. Wang, S. Fan, M. Dong, Z. Ye, X. Peng, *Chem. Eng. J.* **2022**, *430*, 133086.
[30] Y. L. Liu, Y. Y. Zhou, Y. X. Lin, G. Z. Jia, *Results Phys.* **2022**, *38*, 105590.
[31] A. Pradyasti, H. T. Hoang, K. T. Lim, M. H. Kim, *J. Alloys Compd.* **2022**, *896*, 163062.

[32] X. Chen, J.-J. Li, X. Chen, S.-C. Cai, E.-Q. Yu, J. Chen, H. Jia, *ACS Appl. Nano Mater.* **2018**, *1*, 2971.
[33] L. Pei, X. Wang, H. Zhu, H. Yu, S. Bandaru, S. Yan, Z. Zou, *ACS Appl. Mater. Interfaces* **2023**, *15*, 51300.
[34] M. Bilal, M. Sultan, F. Majeed, M. Farooq, U. Sajjad, S. M. Ibrahim, M. U. Khan, S. Azizi, M. Y. Javaid, R. Ahmad, *Sustainability* **2022**, *14*, 12582.
[35] P. Hu, T. S. Wang, J. W. Zhao, C. J. Zhang, J. Ma, H. P. Du, X. G. Wang, G. L. Cui, *ACS Appl. Mater. Interfaces* **2015**, *7*, 26396.
[36] B. Y. Xing, J. G. Zhao, S. Jiang, M. J. Pang, Q. L. Pan, Y. Geng, G. B. Ma, Z. Li, P. D. Han, *Synth. Met.* **2021**, *271*, 116638.
[37] Y. Zhang, H. R. Guo, X. P. Li, J. Du, W. L. Ren, R. Song, *Chem. Eng. J.* **2021**, *404*, 126483.
[38] O. I. Lebedev, F. Millange, C. Serre, G. Van Tendeloo, G. Ferey, *Chem. Mater.* **2005**, *17*, 6525.
[39] H. Khajavi, H. A. Stil, H. P. C. E. Kuipers, J. Gascon, F. Kapteijn, *ACS Catal.* **2013**, *3*, 2617.
[40] A. Entezari, O. C. Esan, X. H. Yan, R. Z. Wang, L. An, *Adv. Mater.* **2023**, *35*, 40.
[41] J. Canivet, J. Bonnefoy, C. Daniel, A. Legrand, B. Coasne, D. Farrusseng, *New J. Chem.* **2014**, *38*, 3102.
[42] M. Tatlier, G. Munz, G. Fueldner, S. K. Henninger, *Microporous Mesoporous Mater.* **2014**, *193*, 115.
[43] A. Khutia, H. U. Rammelberg, T. J. Schmidt, S. K. Henninger, C. Janiak, *Chem. Mater.* **2013**, *25*, 790.
[44] W. Zhao, W.-Q. Huang, M. Li, Z. Huang, *Nano* **2019**, *14*, 67.
[45] X. T. Zhang, F. Q. Li, J. X. Ren, Z. Z. Guan, L. J. Zhang, H. J. Feng, X. Hou, C. Ma, *J. Nanopart. Res.* **2019**, *21*, 105.
[46] A. Ma, H. J. Cong, H. X. Deng, *Green Energy Environ.* **2022**, *7*, 575.
[47] H. Kim, S. R. Rao, M. LaPotin, S. Lee, E. N. Wang, *Int. J. Heat Mass Transfer* **2020**, *161*, 120253.